

PEER-REVIEWED ARTICLE

ASSESSMENT OF STRUCTURE FROM MOTION (SfM) PROCESSING PARAMETERS ON PROCESSING TIME, SPATIAL ACCURACY, AND GEOMETRIC QUALITY OF UNMANNED AERIAL SYSTEM DERIVED MAPPING PRODUCTS

Mr. Adam Benjamin

Geomatics Specialist, University of Florida Geomatics Program, Fort Lauderdale R.E.C., Fort Lauderdale, FL

Mr. Dennis O'Brien

MTA-Long Island Rail Road, Queens, NY

Dr. Grenville Barnes

Professor, University of Florida Geomatics Program, Gainesville, FL

Dr. Benjamin Wilkinson

Assistant Professor, University of Florida Geomatics Program, Gainesville, FL

Mr. Walter Volkmann

President, Micro Aerial Projects L.L.C., Gainesville, FL

ABSTRACT

As unmanned aerial system (UAS)-related mapping applications grow in number, a corresponding demand for enhancing field to finish UAS mapping workflows is at the forefront of the geospatial industry. This study investigates the impact processing parameter selection used in UAS multi-view stereo (MVS) photogrammetry processing has on the spatial accuracy and geometric quality of UAS-derived orthophotos and digital elevation models. The goal is to temporally optimize the semi-automated workflow by applying an understanding of the tradeoffs between parameter values and accuracy/quality metrics associated with the derived geospatial datasets. With 48 trials using the UAS-MVS representative software package, PhotoScan, results show that less rigorous structure from motion (SfM) processing parameters, specifically alignment and dense cloud generation parameters, can provide time savings without sacrificing the spatial accuracy of UAS-derived mapping products in low to moderate topographic relief areas. Lower 'quality' settings in the dense cloud generation phase led to the most significant time savings. When considering geometric quality in addition to spatial accuracy, reducing the alignment 'accuracy' and the number of key points does not impact the spatial accuracy of the resultant geospatial datasets.

I. Introduction

Through a combination of hardware and software designed to automatically collect geospatial data from an aerial platform over a user specified area, unmanned aerial systems (UAS) are a rapidly evolving technology with applications across numerous disciplines (Colomina & Molina, 2014; Pajares, 2015). New investigations of UAS technology for aerial mapping that were previously cost-prohibitive at smaller project scales emerged from development of cost-effective mapping sensors (e.g., consumer grade off-the-shelf (COTS) digital cameras) and user friendly image processing software utilizing structure-from-motion (SfM) and photogrammetric techniques (Sauerbier, Siegrist, Eisenbeiss, & Demir, 2011). Multi-view 3D reconstruction or multi-view stereo (MVS) photogrammetry algorithms provide the foundation for these hybrid SfM/photogrammetry software packages (Harwin & Lucieer, 2012). UAS-MVS derived mapping products are capable of filling a niche in the rapid collection of geospatial datasets at smaller project scales with greater temporal resolution and higher spatial resolutions than conventional aerial surveys or satellite imagery analyses (Casella et al., 2016; Messinger, Asner, & Silman, 2016). Further, Gerke and Przybilla (2016) summarized the main advantages of mapping with UAS over manned aircraft using three concepts: 1) flexibility through highly individualized flight patterns, 2) higher image resolution, and 3) ease of use due to minimal training requirements.

For geospatial professionals working on these smaller project scales, the typical platform is a small UAS (sUAS) (Colomina & Molina, 2014). The sUAS definition varies depending upon the aviation authority. For example, sUAS weigh less than 55 lbs. (24.95 kg) per the Federal Aviation Administration (FAA) in the United States (FAA, 2016) and weigh less than 20kg without fuel per the Civil Aviation Authority (CAA) in the United Kingdom (CAA, 2016). For most commercial mapping applications, sUAS weigh significantly less than these upper weight thresholds. The term “system” in “UAS” refers to the ground-based hardware and crew, airborne platform, and sensor suite used in the mapping process. Two primary sUAS sensor suite categories exist: remote sensing and positioning. The remote sensing category includes both passive (e.g., the aforementioned COTS digital cameras) and active (e.g., LiDAR) sensors that capture imagery and spatial data for the resultant mapping products. Positioning sensors provide navigation for the UAS and estimates of sensor locations can be used for processing the imagery. The small size of the UAS, correspondingly smaller format size of UAS imaging sensors, and lower altitudes result in smaller ground area captured per image relative to conventional aerial imagery from manned aircraft or satellites. Further, UAS-MVS algorithms require more image overlap (Turner, Lucieer, & Wallace, 2014) in order to properly reconstruct the imaged scene in three dimensions than classical photogrammetric methods (Wolf & Dewitt, 2000). Thus, UAS field operations acquire larger quantities of high resolution images for image processing. Depending upon the project area, the imaging sensor used, the mission altitude, and the processing parameters, UAS-MVS image processing can take over a day with high-end computers (Tavani et al., 2014). These long processing times can significantly reduce efficiency of UAS mapping operations.

Using high resolution UAS imagery to map small project areas successfully is a confluence of hardware enhancements (e.g., miniaturization for UAS field operations) and software advancements (e.g., robust algorithms that incorporate computer vision and photogrammetric principles). Low cost sensors capturing imagery for high resolution geospatial datasets on an as-needed basis stimulate growth in the variety and number of UAS mapping applications. Tavani et al. (2014) noted that these factors enabled a larger proportion of geoscientists to use these SfM-generated geospatial datasets because the barriers to utilization (e.g., cost, expertise) are much lower than existing technologies such as LiDAR and satellite imagery. For example, Fonstad et al. (2013) showed that SfM generated datasets have a spatial accuracy that compares favorably to aerial LiDAR datasets at a fraction of the sensor and acquisition costs for geomorphological applications. In forestry applications, Wallace et al. (Wallace, Lucieer, Malenovský, Turner, & Vopěnka, 2016) also showed that SfM generated datasets could be used to adequately characterize vertical vegetation structure relative to LiDAR at a much lower price point. When compared to satellite imagery acquisition, (Panque-Gálvez, McCall, Napoletano, Wich, & Koh, 2014) summarized the cost benefits of using drones for on demand imagery acquisition in forested communities. Further, Colomina and Molina (2014) address the widespread adoption of UAS technology by summarizing the increase in volume of annual UAS-related peer reviewed publications from 2005 to 2013. Even as adoption of UAS-MVS technology increases, significant hurdles still exist. One of the most critical obstacles to enhanced efficiency in the UAS mapping workflow is the computer resource intensive nature of UAS-MVS software (Barnes & Volkmann, 2015; Dietrich, 2016; Turner et al., 2014). Thus, UAS image processing time efficiency is a research area in need of further exploration.

For UAS-MVS image processing, users choose from a multitude of hardware/software options. Some users access high powered servers in a cloud processing environment while others rely on consumer grade laptop specifications. The hardware/software choices greatly influence UAS-MVS processing time. Turner et al. (2014) investigated three potential SfM processing solutions: 1) a commercial software package on a high end desktop computer, 2) an open source software package in a local server environment, and 3) a commercial cloud processing solution. The authors found that processing efficiency depended on using multiple central processing units (CPUs) (i.e., commercial software had multi-CPU ability while open source software did not have that functionality). Additionally, internet upload speeds greatly impacted overall processing time from field to finish for the cloud based processing solution (Turner et al., 2014). In some applications such as cadastral mapping in developing countries (Barnes & Volkmann, 2015), cloud based processing solutions are not feasible due to the large size of data sets and the lack of reliable internet connections. Thus, the optimization of UAS-MVS processing parameters for local computer processing is necessary to generate quality geospatial datasets in a time efficient manner.

A systematic approach to UAS-MVS processing parameter selection is still evolving in the literature. Previous processing parameter approaches with a common SfM processing solution, Agisoft Photoscan (Agisoft, 2016), tended to either 1) briefly mention a trial and error method (Gross & Heumann, 2016; Puliti, Olerka, Gobakken, & Næsset, 2015; Turner et al., 2014), 2) select parameters for optimal accuracy regardless of processing time (Messinger et al., 2016), or 3) base parameter selection on user manual recommendations (Casella et al., 2016; Dandois & Ellis, 2013; Puliti et al., 2015; T. N. Tonkin, Midgley, Graham, & Labadz, 2014). More recent studies have focused on improving UAS data acquisition techniques (e.g., flight planning (Carbonneau & Dietrich, 2016; Fonstad et al., 2013; Mike R. James & Robson, 2014), configuring ground control networks (Clapuyt, Vanacker, & Van Oost, 2016; M. R. James, Robson, d'Oleire-Oltmanns, & Niethammer, 2017; Toby N. Tonkin & Midgley, 2016) and refining camera calibration methods for non-metric cameras (M. R. James et al., 2017; Mike R. James & Robson, 2014). The adoption of these methods going forward will lead to more accurate and complete SfM-derived geospatial datasets. However, a study emphasizing a systematic approach to parameter selection for enhancing processing time efficiency without sacrificing accuracy or quality is still lacking.

The primary objective of this paper is to investigate the impact that SfM/UAS-MVS processing parameters have on spatial accuracy and geometric quality of UAS-derived geospatial datasets. Spatial accuracy, described in greater detail in Section 2.6, assesses the horizontal and vertical difference between ground truth data and the final mapping products. Meanwhile, geometric quality, described in greater detail in Section 2.7, assesses the qualitative fidelity of the derived orthophoto mosaics in terms of distinguishing and identifying features within the imagery. The goal is to temporally optimize the semi-automated workflow by applying an understanding of the tradeoffs between parameter values and accuracy/quality metrics associated with the UAS-derived geospatial datasets.

2. Materials and Methods

2.1. UAS Mapping Workflow

To efficiently obtain quality geospatial datasets from UAS mapping platforms, a workflow similar to Figure 1 needs to be established and followed. The UAS mapping workflow has three phases: 1) mission planning/field operations, 2) aerotriangulation/processing, and 3) geospatial dataset creation. The first phase involves the necessary UAS mapping data collection techniques for both the establishment of ground control and the airborne operations. The second phase covers the integration of photogrammetric principles such as aerotriangulation (i.e., determination of XYZ coordinates of individual points based on photo coordinate measurements (Wolf & Dewitt, 2000)) with SfM processes. Lastly, the generation of the UAS-derived geospatial datasets occurs in the third phase.

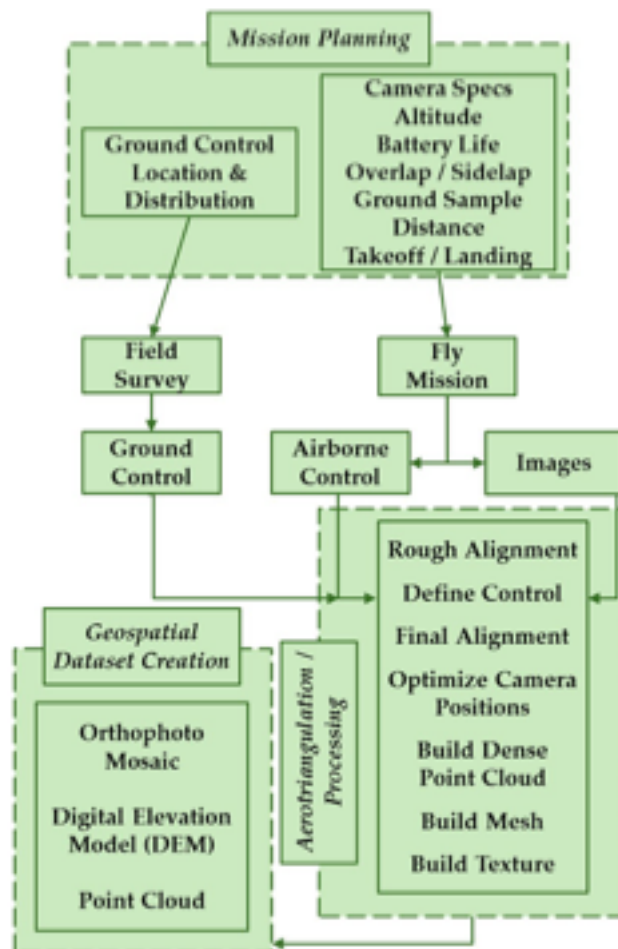


Figure 1: Unmanned aerial systems mapping workflow

2.2. Study Site

The mission planning and field operations based components of the UAS mapping workflow are location dependent. Physical site conditions, airspace regulations, weather conditions, and equipment capabilities factor into operational considerations. The 3.5 ha study area, outlined in blue in Figure 2, was located in Alachua County, FL, USA. The study area contained a high point density of field surveyed three-dimensional and vertical-only ground control relative to areas outside of the study area boundaries. Thus, the authors selected the study area for two reasons: 1) the availability of high density ground control and 2) the reduction of data storage (e.g., 122 images for the study area versus 314 images for the entire site) needed to conduct the numerous trials in this study. While study area selection affected absolute processing time, it did not affect relative processing times amongst the trials. The relative impact each processing parameter had on processing time within and across trials was preserved. Section 2.5 discusses the processing parameters and trials in greater depth.

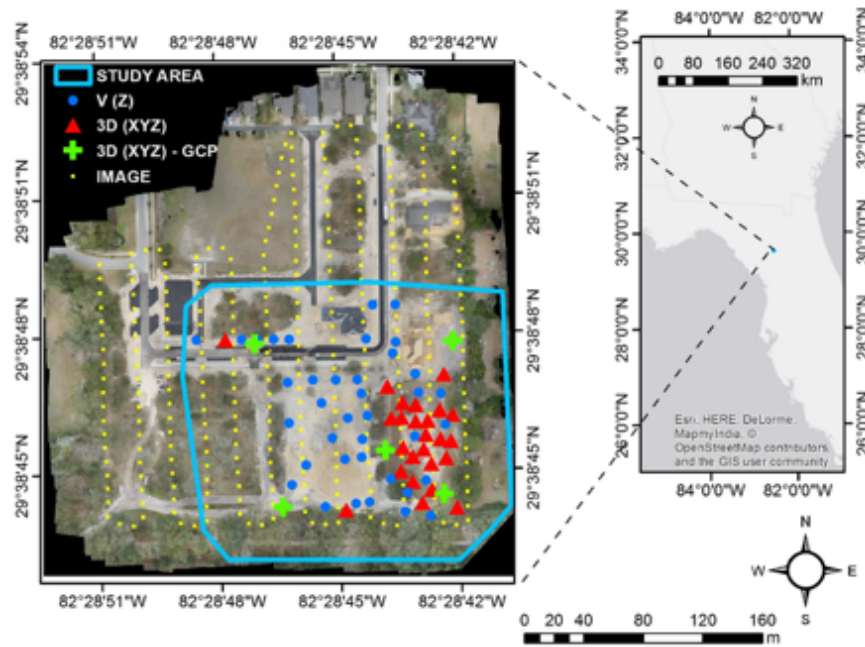


Figure 2: The study area (blue polygon) in Alachua County, FL, USA has vertical ground control (blue circles) and 3D ground control (red triangles) for spatial accuracy evaluation, 3D ground control (green crosses) for georeferencing the imagery, and approximate image locations (yellow squares) for showing the flight acquisition pattern.

2.3. Field Data Collection

One UAS flight with a MAP-M4 multirotor quadcopter airframe as shown in Figure 3 was flown over the entire site on February 15, 2016. The sUAS had a single-frequency code based GNSS positioning sensor that navigated the aircraft over a predetermined flight plan. The yellow squares in Figure 2 show the approximate locations where nadir images were acquired along the north-south flightline. The imaging sensor was a 16mm focal length Sony a6000 camera with an effective image resolution of 6000×4000 pixels. Given an altitude above ground level (AGL) of about 55m, the ground resolution of the resultant sUAS imagery was ~ 1.25 cm/pixel.



Figure 3: MAP-M4 multirotor quadcopter UAS

Five field surveyed aerial targets were used as ground control points for georeferencing the imagery and resultant geospatial datasets. These targets, as shown in Figure 4, consisted of four alternating black and white triangles intersecting at the center of the 25 cm square targets. Field survey observations also included measurements to additional horizontal aerial target check points (e.g., 10.5 cm white circular disks) and vertical only check points. The aerial targets provided photo identifiable features used as three-dimensional (i.e., both horizontal and vertical) check points when overhead vegetation did not obscure the targets. Lacking photo-identifiable features, the high accuracy vertical only check points comprised the primary reference data in the digital elevation model (DEM) spatial accuracy evaluation. Surveying with both V-Map dual frequency GNSS receivers and a Spectra Precision Focus 35 robotic total station as shown in Figure 4 enabled establishment of the entire ground control point (GCP) network. Two Alachua County corner markers with published Florida North State Plane Coordinates provided the geodetic control onsite. Static GNSS survey observations and subsequent GNSS post processing with RTKLIB software (RTKLIB, 2017) verified the observed baseline distance matched the computed baseline distance from the published coordinates. Using this geodetic control, redundant robotic total station measurements yielded a horizontal and vertical precision of less than 0.01 m for control and check point data.



Figure 4: Black and white square aerial targets (a) were field surveyed using a robotic total station (b) and GNSS surveying.

2.4. Computer Resources

The “aerotriangulation/processing” and “geospatial dataset creation” phases of the UAS mapping workflow in Figure 1 require substantial computer resources to process high resolution sUAS mapping products (Verhoeven, 2011). A 64-bit Windows 7 desktop computer with a 3.70 GHz Intel Xeon CPU E5-1620 processor, 48GB of RAM, a 1TB 7200 RPM hard drive, and a NVIDIA Quadro K4000 graphics processing unit (GPU) performed all data processing during the study. These specifications meet or exceed the Agisoft recommended configuration of a 64-bit Windows OS, Intel i7 processor, 12GB RAM, and a NVIDIA GeForce 8xxx series graphics card (Agisoft, 2016).

There are several software packages capable of processing SfM-MVS datasets including Agisoft Photoscan (Agisoft, 2016), Pix4D (Pix4D, 2016), and VisualSfM (Wu, 2016). The authors chose Photoscan (v1.2.5 build 2614) as the representative software package for this study because: 1) it is widely used within both academia and industry for generating UAS-derived geospatial datasets (Carbonneau & Dietrich, 2016; Casella et al., 2016; M. R. James et al., 2017; Javernick, Brasington, & Caruso, 2014; Puliti et al., 2015; Tavani et al., 2014; Toby N. Tonkin & Midgley, 2016; Turner et al., 2014; Verhoeven, 2011), 2) it is an attractive option for new UAS mapping technology adopters due to the extensive software user community (<http://www.agisoft.com/forum/>) and manageable purchase price for small organizations (Gross & Heumann, 2016), and 3) it has extensive reporting features related to processing time (Agisoft, 2016). Following the Agisoft Photoscan User Manual’s recommendations for optimal performance, one central processing unit (CPU) core was deactivated for each GPU in use (Agisoft, 2016). Due to Agisoft support of OpenCL acceleration during the depth maps reconstruction phase of building dense point clouds (Agisoft, 2016),

processing speed can increase substantially using the multiple GPU/CPU approach (Turner et al., 2014; Verhoeven, 2011). Thus, the optimal processing unit configuration for this system was seven CPUs and one GPU.

2.5. SfM Processing

In the aerotriangulation/processing phase of the sUAS mapping workflow shown in Figure 1, the seven distinct steps in the Agisoft Photoscan workflow are: (1) rough alignment, (2) control definition, (3) final alignment, (4) camera position optimization, (5) dense point cloud generation, and optionally, (6) mesh generation, and (7) texture generation. These processes (6 and 7) enable the generation of digital elevation/surface models and the orthophoto mosaics for traditional geospatial data products; however, these products may not be required for every research application.

The following is a brief description of the SfM processing workflow within Photoscan. Additional details can be obtained from the Agisoft user manual (Agisoft, 2016) and previous literature on SfM processing (Casella et al., 2016; Puliti et al., 2015; Verhoeven, 2011). Upon importing all images into Photoscan, the rough alignment process benefited from the manual control definition of three unique GCPs. Manual control definition entailed selecting the center of the photo-identifiable field surveyed ground control where the GCP was visible. Each GCP was selected in two separate images. Rough alignment stitched the images together into a block using tie points, which are described in more detail in Section 2.5.1.

While control definition in an automatic or semi-automatic manner is possible depending upon the photo-identifiable aerial targets and the centroid defining algorithms (Harwin & Lucieer, 2012), the only manually completed step in the sUAS workflow within Photoscan v1.2.5 was control definition. While Photoscan now supports coded targets for automatic aerial target identification, this study did not use this option. The rough alignment step expedited additional manual control definition by enabling the software to display approximate locations of all targets in the images based on the location of the 3 GCPs used to georeference the image block in the rough alignment step.

For all trials, five three-dimensional GCPs provided the georeferencing for the final geospatial datasets. As shown by the green crosses in Figure 2, the GCP spatial configuration approximates a bounding square with a point in the middle. Based on previous internal research, this spatial configuration provided the optimal configuration for a five point ground control network with diminishing returns on spatial accuracy for additional control points used in the georeferencing. Recent literature discusses optimal GCP distribution in greater depth and provides support for this GCP configuration through emphasis on strong network geometry with a spatial distribution spanning the survey area (M. R. James et al., 2017). Specifically, Tonkin and Midgley (2016) found that 4 or more GCPs well distributed throughout the study area provided vertical spatial accuracies consistent with the positional quality of the measurements used to determine the GCP coordinates.

For processes (3-7), an investigation into reducing Photoscan processing parameter rigor from the default settings shown in Table 1 and the corresponding effects of these altered settings on spatial accuracy, geometric quality, and processing time ensued. Table 2 shows an example of the processing time for this study site using Photoscan default parameters (Agisoft, 2016). Of the remaining five steps in the processing phase, final photo alignment (step 3) and dense cloud generation (step 5) accounted for over 95% of total processing time. Therefore, thorough investigation from here on focused primarily on alteration of the corresponding parameters for those two steps.

Table 1: Default Agisoft Photoscan processing parameters

Alignment	
Accuracy	High
Pair preselection	Disabled
Key point limit	40000
Tie point limit	4000
Constrain features by mask	No
Camera Optimization	
Parameters	f, cx, cy, k1-k3, p1, p2
Dense Point Cloud Generation	
Quality	High
Filtering mode	Moderate
Mesh Generation	
Surface type	Height field
Source data	Dense Cloud
Interpolation	Enabled
Quality	High
Depth filtering	Moderate
Texture Generation	
Mapping mode	Adaptive orthophoto
Blending mode	Mosaic
Texture size	4,096 x 4,096
DEM Generation	
Source data	Dense cloud
Interpolation	Enabled
Orthomosaic Generation	
Channels	3, uint8
Blending mode	Mosaic
Surface	Mesh
Enable color correction	No

Table 2: Processing time for the study area using default Photoscan parameter settings

#	Parameter	Proc. Time (min)	Proc. Time (% Total)
1	Final Alignment	41.88	17%
2	Camera Position Optimization	0.03	0%
3	Dense Cloud Generation	191.25	79%
4	Mesh Generation	4.57	2%
5	Texture Generation	5.18	2%

2.5.1. Final Alignment & Dense Cloud Generation

Depending upon the project size and the parameters selected in Table 3, final photo alignment processing time can vary from a few minutes to days. Thus, a balance between alignment time and generated mapping dataset accuracy is necessary. Table 3 described the four primary parameters used in the alignment process: (1) ‘accuracy’, (2) ‘pair preselection’, (3) ‘key point limit’, and (4) ‘tie point limit’. The ‘accuracy’ parameter does not denote the spatial accuracy of the alignment. Instead, ‘accuracy’ in the context of alignment for the Photoscan processing parameters defines the spatial resolution of each image used in the alignment process (e.g., a higher ‘accuracy’ value means an image with a higher spatial resolution is used). The ‘pair preselection’ parameter enables the use of precise camera exposure stations. Camera exposure positioning data was not available in the EXIF metadata for the images in this study. Enabling ‘pair preselection’ is recommended when the data is available as it improves processing speed in the alignment process. ‘Key point limit’ defines the maximum number of feature points to collect in each image while ‘tie point limit’ defines the maximum number of points matched across images.

Table 3: Alignment parameters in Agisoft Photoscan. The ‘Evaluated’ column indicates whether an alignment parameter was altered for evaluation during the processing trials.

Parameter	Value	Interpretation	Evaluated
Accuracy	Highest	Upscales image resolution by 4	Yes
	High	Original image resolution	Yes
	Medium	Downscales image resolution by 4	Yes
	Low	Downscales image resolution by 16	Yes
	Lowest	Downscales image resolution by 64	Yes
Pair preselection	Disabled	Ground control only	Yes
	Reference	Airborne control enabled	No
Key point limit	XXXXX1	Upper threshold of feature points per image	Yes
Tie point limit	XXXX	Upper threshold of matching points per image	Yes

1 - XXXXX denotes a 5 digit integer number

From the summary of dense cloud generation processing parameters in Table 4, the primary parameter is dense point cloud ‘quality’. Similar to the alignment process, ‘quality’ corresponds to image resolution. The ‘depth filtering’ parameter indicates which algorithm is used to mitigate artifacts based on knowledge of the scene geometry. The authors chose ‘moderate depth filtering’ based on past experience with similar sites and to provide a balance between the ‘mild depth filtering’ approach that preserved more details with a subsequent increase in outlier data and the ‘aggressive depth filtering’ approach with cleaner data and fewer preserved details.

Table 4: Dense cloud generation parameters in Agisoft Photoscan. The ‘ultra high quality’ setting was tested against the ‘high quality’ setting by keeping the remaining SfM processing parameters the same. Testing results yielded a more than six fold increase in processing time (‘ultra high quality’ total time > 20 hrs). Thus, the ‘ultra high quality’ value was not evaluated for consideration as an optimal parameter.

Parameter	Value	Interpretation	Evaluated
Quality	Ultra High	Original image resolution	No
	High	Downscales image resolution by 4	Yes
	Medium	Downscales image resolution by 16	Yes
	Low	Downscales image resolution by 64	Yes
	Lowest	Downscales image resolution by 256	No
Depth filtering	Aggressive	Filters points because meaningful small details are not in subject area	No
	Moderate	Balance between aggressive and mild approaches	Yes
	Mild	Filters fewest points to preserve small details in subject area	No

The relationship between the different alignment and dense cloud parameters is explored herein through 48 separate trials. To identify the parameters that provided the best tradeoff between spatial accuracy and processing time, the experimental setup included the following characteristics. Each trial used the same five GCP configuration described earlier and shown in Figure 2. Further, the camera position optimization, mesh generation, texture generation, DEM generation, and orthophoto mosaic generation parameters were the same for all trials. Generated orthophoto mosaics and DEMs had spatial resolutions of 1.2 cm/pixel and 2.4 cm/pixel, respectively. The fourth column in Table 3 and Table 4 indicate whether a particular parameter was modified during the trials. Different combinations of ‘key point limit’ and ‘tie point limit’ used in the trials are shown in Table 5. Combination 1 with a 40,000 ‘key point limit’ (KP) and a 4,000 ‘tie point limit’ (TP) is the default setting for KP and TP alignment settings within Photoscan (Agisoft, 2016). Using the default 40,000 KP setting was a frequent occurrence within the literature (Casella et al., 2016; Gross & Heumann, 2016; M. R. James et al., 2017; Messinger et al., 2016; Puliti et al., 2015; Verhoeven, 2011). Combination 7 and combination 8 were included after considering experience with photogrammetric ratios of feature points to matching points as well as DEM errors with small tie point limits discussed in the results section.

Table 5: ‘Key point limit’ and ‘tie point limit’ combinations used during trials

#	Key Point Limit	Tie Point Limit
1	40000	4000
2	40000	2000
3	40000	1000
4	20000	2000
5	20000	1000
6	20000	500
7	8000	5000
8	4000	2500

2.6. Spatial Accuracy Assessment

The 2015 American Society of Photogrammetry and Remote Sensing (ASPRS) Positional Accuracy Standards for Digital Geospatial Data provide spatial accuracy reporting metrics related to horizontal and vertical accuracy (ASPRS, 2015). The root mean squared error (RMSE) is the primary spatial accuracy metric that computes the difference between a known/true value and an observed value. Easting RMSE (RMSEX), northing RMSE (RMSEY), horizontal RMSE (RMSE_H), and horizontal accuracy at a 95% confidence level (HZ95) are horizontal absolute accuracy metrics derived from comparing SfM-generated geospatial datasets to field surveyed ground control. Likewise, vertical RMSE (RMSE_Z) and vertical accuracy at a 95% confidence level (V95) are the vertical absolute accuracy metrics.

To compute the GCP observed values, the Editor toolbar in ArcGIS 10.4 for Desktop (ArcMap) software from Environmental Systems Research Institute (ESRI) (ESRI, 2016) enabled the manual selection of the center of photo identifiable targets on each orthophoto mosaic. After digitizing all photo identifiable GCPs for each trial, a Python script used the ArcPy package from ESRI and the Field Calculator tool to obtain the manually measured coordinates. All horizontal coordinates were in the Florida North state plane projection, NAD83 (2011) horizontal datum. A comparison between these observed GCP coordinates and the field-surveyed GCP coordinates determined horizontal coordinate differences. Likewise, a comparison between the high resolution digital elevation model (DEM) derived from the sUAS data and the field-surveyed GCP heights formed the basis of the vertical accuracy evaluation. All vertical coordinates were in the same vertical datum, NAVD88 (GEOID 12B). The spatial accuracy metrics used the horizontal and vertical coordinate differences to compute the RMSE metrics. If necessary, the RMSE data is available to communicate the spatial accuracy in other positional guidelines such as Accuracy Standards for Large Scale Maps (ASPRS, 1990), Vertical Accuracy Reporting for LiDAR Data (Flood, 2004), or Geospatial Positioning Accuracy Standards: National Standard for Spatial Data Accuracy (NSSDA) (FGDC, 1998) standards.

Summary statistics including mean, standard deviation, skew, and kurtosis were calculated for each of the spatial accuracy metrics: easting RMSE (RMSEX), northing RMSE (RMSEY), horizontal RMSE (RMSE_H), horizontal accuracy at a 95% confidence level (HZ95), vertical RMSE (RMSE_Z), and vertical accuracy at a 95% confidence level (V95). Per the Positional Accuracy Standards for Digital Geospatial Data (ASPRS, 2015), skewness and kurtosis are recommended to show the normality of the error distribution and the frequency of extreme errors. In general, skewness assesses the symmetry of the error distribution. Kurtosis assesses how much of the variance is the result of extreme deviations relative to modest sized deviations.

2.7. Geometric Quality Assessment

While spatial accuracy is critical for quantifying the uncertainty in the measurement of features in sUAS-derived geospatial datasets, geometric quality (i.e., image quality) assesses the qualitative fidelity of the derived orthophoto mosaics in terms of distinguishing and identifying features within the imagery. Gross and Heumann (Gross & Heumann, 2016) used image artifacts (e.g., outliers) and image blur to assess image quality. Their assessment methodology was adopted herein, where 100 points were randomly placed throughout the orthophoto mosaic. Buffers of 2.5m were drawn around each point creating search area circles with a 5m diameter. Figure 5 shows the random distribution pattern of these geometric quality assessment circles. Circle locations spanned a variety of land cover classes including bare ground, trees, structures, and roads. These circles were examined manually within ArcMap software for the presence of image artifacts and image blur. While image artifacts are regions of misaligned pixels within the image that have distinct visible errors, image blur is simply an area of the orthophoto mosaic that has a blurred appearance due to either input image quality or image processing (Gross & Heumann, 2016). The results are reported in a binary format as either presence (1) or absence (0) for each circle. In addition, data voids and the dominant land cover class were also noted. Figure 6 is an example of the presence of both an image artifact and image blur for one of the 100 samples. The same sample areas were used for analysis across the trials. Finally, Figure 7 shows a variety of land cover classes illustrating the presence of image artifacts or image blur.

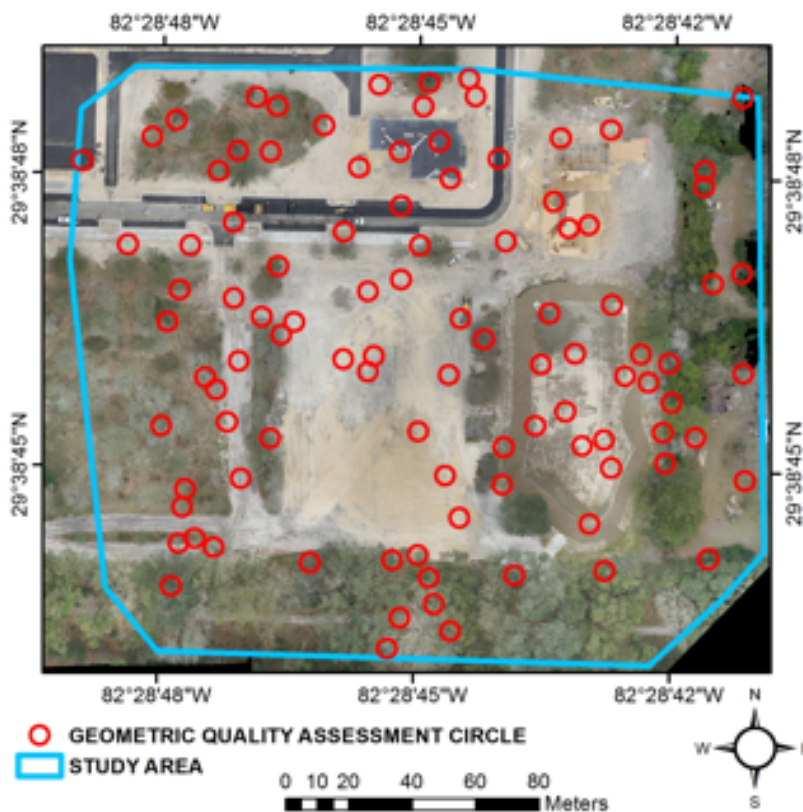


Figure 5: Random distribution of geometric quality assessment circle locations for identifying the presence of image artifacts, image blur, and data voids.

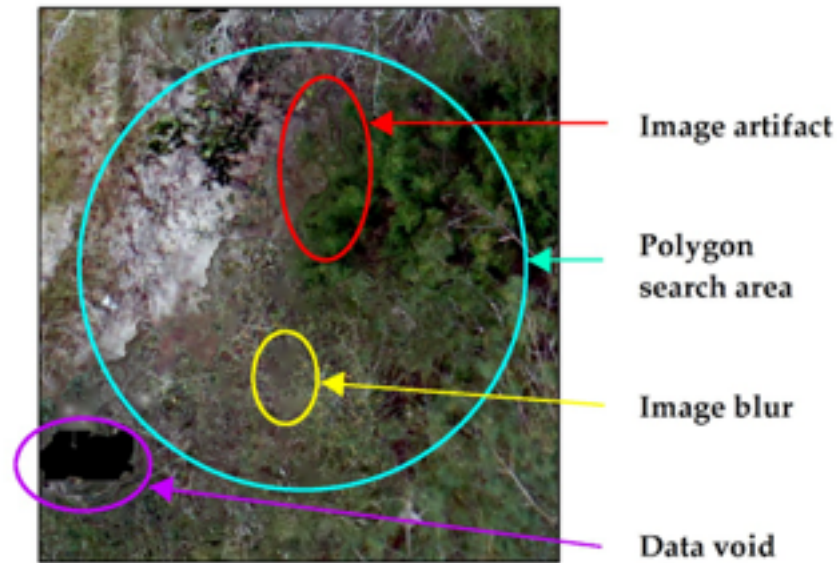


Figure 6: Example of geometric quality assessment 5m diameter circle (blue) showing an image artifact (red), image blur (orange), and a data void (purple). Note that the data void occurs outside of the assessment polygon.

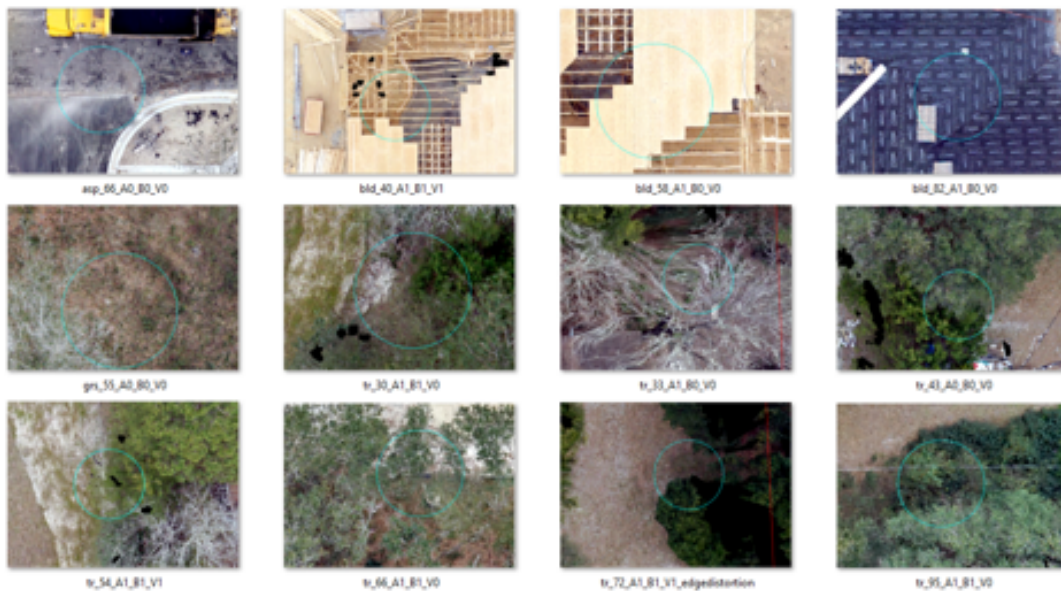


Figure 7: Examples of geometric quality assessment polygons organized by dominant land cover class: asphalt (asp), building (bld), grass (gr), and tree (tr). For the image labels, ‘A1’ indicates the presence of at least one image artifact within the circle, ‘B1’ indicates the presence of image blur within the circle, and ‘V1’ indicates a data void within the circle. Meanwhile, ‘A0’ indicates the absence of image artifacts within the circle.

3. Results

3.1. Spatial Accuracy Assessment Results

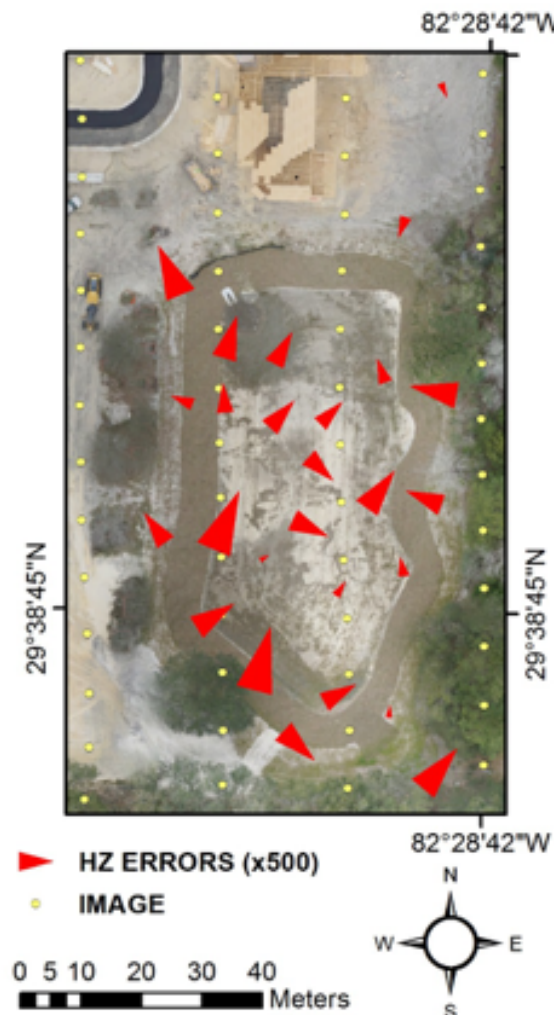
Summary statistics for the horizontal and vertical spatial accuracy assessment of the 48 trials are shown in Table 6 and Table 7, respectively. These results are displayed graphically in Figure 9(a-b). The mean horizontal accuracy assessment statistics in Table 6 (a-b) for each of the horizontal metrics show that the mean horizontal accuracy is about 1 cm with mm-level variation in the standard deviation of the mean across the 48 trials. Thus, horizontal accuracy is of a similar magnitude (~1 cm) to the error associated with the ground control survey described in Section 3.3. The low R-squared values in Figure 9a derived from the linear regression implemented in the Data Analysis ToolPak within Microsoft Excel supports the notion that horizontal spatial accuracy has a significant, weak negative correlation (coefficient = -0.0000049; p = 0.004) with processing time. Therefore, horizontal spatial accuracy is minimally affected by higher ‘accuracy’ or ‘quality’ Photoscan parameters causing the longer processing times. Thus, the lower ‘accuracy’ alignment parameters can be used with shorter duration processing times without sacrificing spatial accuracy of the geospatial datasets. Given minimal variation in horizontal spatial accuracy over all trials, the impact of altering the alignment ‘accuracy’, the ‘key point limit’, the ‘tie point limit’, and the dense cloud ‘quality’ has minimal impact on the resultant horizontal spatial accuracy. Further statistical analysis is necessary to parse out if the small variations that are present are due to one or two significant parameters. Lastly, the direction of flight was approximately north-south as shown in Figure 2. Therefore, it is interesting that the along flight line errors in the north-south direction are more normally distributed relative to the cross flight line easting errors which have a larger skew. Upon visual inspection of maps illustrating the spatial variability of horizontal spatial errors in each individual trial, no systematic distortions relating to the north-south flight pattern could be discerned. Figure 8 is an example of a spatial variability map for the default Photoscan settings from Table 1 with directional symbols showing errors scaled by 500. The random spatial pattern of errors found in this map was typical across the trials.

Table 6: Easting (a), northing (a), and horizontal (b) spatial accuracy assessment summary table for 48 trials

(a)								
	Easting Accuracy - RMSEX				Northing Accuracy - RMSEY			
	avg (m)	std dev (m)	skew	kurtosis	avg (m)	std dev (m)	skew	kurtosis
Mean	0.008	0.006	1.50	3.63	0.006	0.004	0.47	-0.04
SD	0.001	0.001	0.74	3.46	0.001	0.001	0.49	1.14
Max	0.010	0.008	3.09	11.62	0.007	0.006	1.94	5.15
Min	0.005	0.004	0.25	-0.93	0.004	0.003	-0.47	-1.31
Range	0.005	0.003	2.84	12.54	0.003	0.003	2.41	6.46

(b)								
	Horizontal Accuracy - RMSER				95% Conf. Level		GCPs	Proc. Time
	avg (m)	std dev (m)	skew	kurtosis	Hz (m)	Hz		
Mean	0.010	0.006	1.17	2.82	0.018	22.0	111.8	
SD	0.001	0.001	0.67	2.42	0.002	0.8	82.3	
Max	0.013	0.009	2.50	8.52	0.022	25	247	
Min	0.009	0.004	-0.25	-0.51	0.016	21	10	
Range	0.004	0.005	2.75	9.03	0.006	4	237	

Figure 8: Spatial variability error map for the default Photoscan settings with directional symbols showing horizontal spatial accuracy errors scaled by 500.



The vertical accuracy assessment statistics in Table 7a for the two vertical metrics show that there is more variation in vertical accuracy than horizontal accuracy. It is known in photogrammetry that vertical accuracy will perform worse than horizontal accuracy due to vertical measurements requiring multiple images (i.e., ray intersections) while horizontal measurements can be made in one image (Wolf & Dewitt, 2000). However, much of the vertical accuracy variation can be attributed to the three outlier trials shown in Figure 9b. Each of these trials used the ‘highest accuracy’ alignment, 20000 ‘key point limit’, and 500 ‘tie point limit’ with varying ‘quality’ dense clouds. Figure 10b shows the errors in the digital elevation model near a building roof. The likely error source is the use of a relatively small number of tie points with upscaled imagery. With an increased number of pixels per image, excessive matching in specific areas of the image could result in an unequal distribution of tie points and, in turn, errors in the alignment. This would affect subsequent processing steps including the digital elevation model generation. With the three trials removed from the testing as shown in Table 7b and Figure 9b, the vertical accuracy variation is more stable across the remaining 45 trials with 2 mm and 4 mm standard deviations for the mean vertical spatial accuracy metrics. With the removal of the 3 outlier trials, a simple linear regression became possible due to dataset normality. The low R-squared value in the vertical accuracy Figure 9b for the 45 trial subset and the corresponding high p-value (0.677) for processing time means processing time does not significantly impact vertical spatial accuracy. Thus, higher ‘accuracy’/‘quality’ processing parameters and longer processing times do not lead to substantial improvements in vertical spatial accuracy.

Table 7: Vertical spatial accuracy assessment summary table for trials. (a) All 48 trials. (b) The 45 remaining trials after removing the three outlying trials.

(a)							
	Vertical Accuracy - RMSEZ			95% Conf. Level		GCPs	Proc. Time
	avg (m)	std dev (m)	skew	kurtosis	V (m)	V	(min)
Mean	0.028	0.031	1.470	5.673	0.055	62.9	111.8
SD	0.008	0.050	1.780	14.979	0.015	0.3	82.3
Max	0.063	0.263	7.769	61.129	0.123	63	247
Min	0.019	0.014	0.312	-0.761	0.037	62	10
Range	0.044	0.249	7.457	61.889	0.086	1	237

(b)							
	Vertical Accuracy - RMSEZ			95% Conf. Level		GCPs	Proc. Time
	avg (m)	std dev (m)	skew	kurtosis	V (m)	V	(min)
Mean	0.026	0.018	1.055	2.026	0.051	62.9	111.9
SD	0.002	0.003	0.748	4.694	0.004	0.3	81.6
Max	0.029	0.027	4.553	29.112	0.057	63	247
Min	0.019	0.014	0.312	-0.761	0.037	62	10
Range	0.010	0.013	4.241	29.873	0.020	1	237

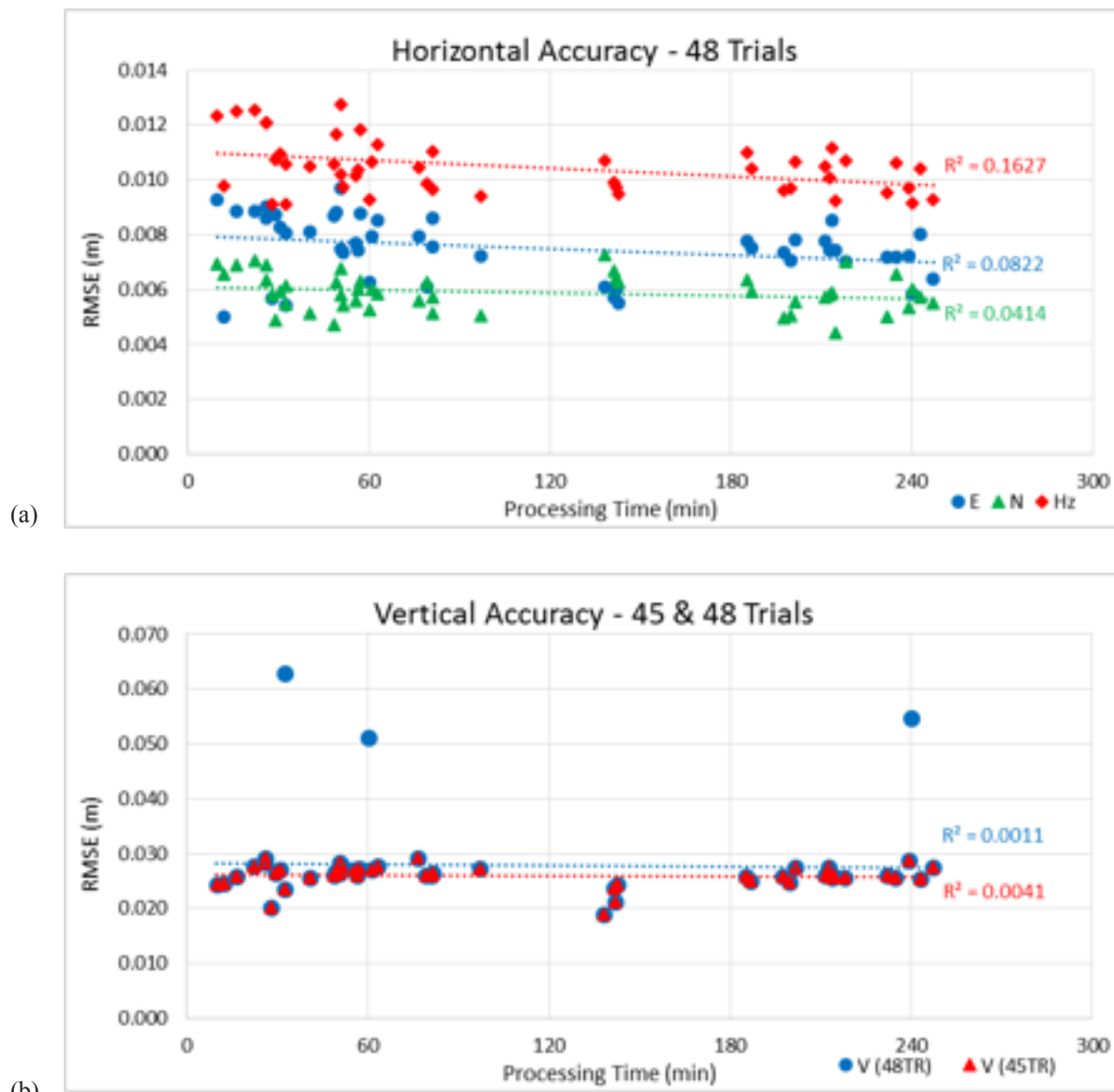


Figure 9: Scatter plot diagrams of the relationship between spatial accuracy assessment results and processing time for trials. (a) Easting, Northing, & Horizontal (b) Vertical – 48 trials & Vertical – 45 trials after removing the three outlying trials

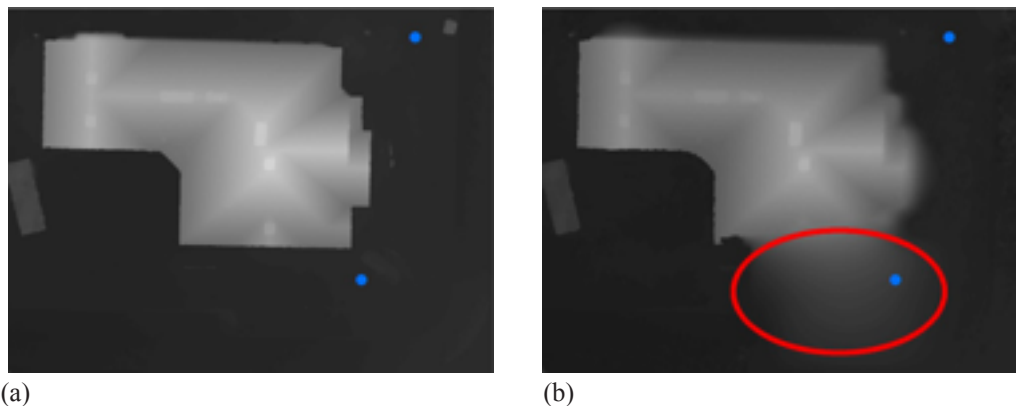


Figure 10: Comparison of normal digital elevation model (a) and digital elevation model (b) created with 'highest accuracy' alignment, 20000 'key point limit', and 500 'tie point limit'. The bright white areas are higher elevations and the darker areas are lower elevations. The red circle shows areas where vertical checkpoints are measuring inaccurate elevations because the edges of the building roof to the east and to the south of the building and the ground are not well defined.

3.2. Geometric Quality Assessment Results

The geometric quality assessment results for selected trials are found in Table 8. A comparison between orthophotos generated with 'medium quality' dense clouds (Trial 13 & Trial 25) and 'high quality' dense clouds was conducted first to analyze the difference in image quality. The R-squared values derived from the linear regressions on the left side of Figure 11 offer statistical support that the shorter processing times from the 'medium quality' dense clouds have a direct correspondence to an increase in the presence of both image artifacts and image blur for the same set of randomly generated circles. The negative coefficients and p-values support the significant correspondence that a decrease in processing time led to an increase in image artifacts (coefficient = -0.070; $p = 0.007$), image blur (coefficient = -0.058; $p = 0.026$), and data voids (coefficient = -0.017; $p = 0.106$).

Thus to preserve the highest image quality, the authors decided to compare only 'high quality' dense clouds based on different 'accuracy' alignments by removing 'low' or 'medium quality' generated dense clouds from consideration. This meant that many of the fastest trial processing times were removed from consideration going forward. Trials 30, 32, 36, 37, 38, and 40 were compared to each other in Figure 11. Differences in image artifact and image blur presence between the three alignment types over the six trials relative to processing time were not significant as shown by the low R-squared values on the right-hand side of Figure 11. Further, the subsequent simple linear regressions statistically supported this lack of significance for image artifacts ($p = 0.753$), image blur ($p = 0.203$), and data voids ($p = 0.300$). Data voids were highest for the 'lowest accuracy' alignment trials, 30 and 32.

Table 8: Geometric quality assessment results for selected trials

#	Alignment 'accuracy'	Key pt. limit	Key pt. limit	Dense cloud 'quality'	N	Image Artifacts	Image Blur	Data Voids	Proc. Time (min)
13	Medium	20000	500	Medium	100	45	42	16	49
25	Medium	40000	1000	Medium	100	46	35	13	79
30	Lowest	4000	2500	High	100	38	30	15	141
32	Lowest	8000	5000	High	100	30	25	14	143
33	Medium	20000	500	High	100	34	26	12	185
36	Medium	4000	2500	High	100	37	31	11	200
37	Low	4000	2500	High	100	33	27	10	201
38	Low	4000	5000	High	100	33	28	15	211
40	Medium	8000	5000	High	100	31	27	12	214
44	Medium	40000	1000	High	100	35	32	13	235

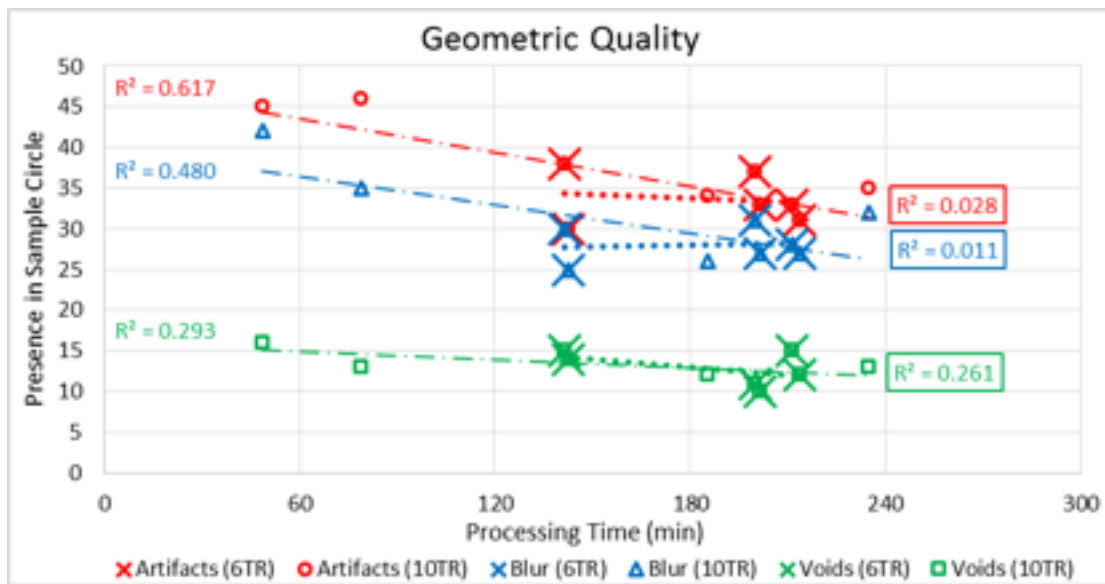


Figure 11: Geometric quality assessment of orthophotos. (a) The dash-dot linear trend lines indicate a direct relationship between presence of image artifacts and processing time for the ten selected trials that include both 'medium' and 'high quality' dense clouds. The respective R-squared values for these dash-dot trend lines are on the left side of the figure. The dot-only linear trend lines indicate the variation in image artifacts and image blur does not correspond to processing time for the six remaining trials after removing the 'medium quality' dense clouds and large 'key point limit' trials. The corresponding R-squared values for these trend lines are on the right side of the figure and outlined.

4. Discussion

Changing the ‘accuracy’ alignment parameter, the ‘key point limit’, the ‘tie point limit’, and the generated dense cloud ‘quality’ parameter provided a wide range of processing times for the generation of the digital elevation model and the orthophoto mosaic. The total processing time for these 48 trials ranged from 10 minutes to 247 minutes (4 hours, 7 minutes). With 122 images used for this study area, total processing time on a per image basis ranged from 5 s/image to 121 s/image. This wide range in processing times yielded minimal changes in either the horizontal or vertical spatial accuracy. The statistical relationship between processing time and spatial accuracy was either significant with weak negative correlation (horizontal) or insignificant (vertical). Thus, substantial time savings can be had if the users’ primary objective is to obtain spatially accurate orthophotos and coarse resolution digital elevation models.

The final alignment ‘accuracy’ parameter and the dense cloud generation ‘quality’ parameter relate to the spatial resolution of the imagery used in the UAS-MVS processing. The range in processing times across the 48 trials supports the direct correspondence in reduced processing time derived from the selection of lower image resolution parameters. Interestingly, the use of higher fidelity image resolution during alignment does not translate to improvements in spatial accuracy.

While ‘high quality’ dense cloud generation takes longer to process than ‘low’ or ‘medium quality’ dense cloud generation, the geometric quality assessment showed that orthophoto mosaic quality is significantly better when using a ‘high quality’ generated dense cloud. Therefore, it is recommended that processing is completed using a ‘high quality’ dense cloud to minimize image artifacts and image blur. Given slight improvements in spatial accuracy using a more traditional ratio of key points to tie points and slightly better data completeness in the visual accuracy assessment (i.e., fewer voids), the optimal settings derived from the 48 trials for a low to moderate topographic relief study area are from Trial 37 and shown in Table 9.

Table 9: Final Photoscan processing parameters for alignment and dense point cloud generation derived from spatial accuracy assessment and geometric quality assessment.

Alignment	
Accuracy	Low
Pair preselection	Disabled
Key point limit	4000
Tie point limit	2500
Constrain features by mask	No
Dense Point Cloud Generation	
Quality	High
Filtering mode	Moderate

Discussion of these results within a broader context of sUAS mapping is critical. Broader contextual considerations include project site characteristics, data acquisition methods, computer resources, software processing, and applications across a variety of disciplines. The remainder of the discussion is split into two sections based on implications for field operations and data processing across multiple disciplines.

4.1. Field operations

Site characteristics and data acquisition techniques have implications on field operation procedures and efficiency. While multiple site variables can potentially affect UAS-derived geospatial datasets, the dominant characteristics of a site are its topography and its land cover. The study area featured herein and shown in Figure 2 is a residential area with low to moderate topographic relief. It contains a variety of land cover including both vegetated areas (e.g., grass, shrubs, dense tree canopy, sparse tree canopy) and improved areas (e.g., roads, structures). Thus, the study area is representative of common land development parcels here in the southeastern United States and other areas worldwide. With the adoption of Part 107 regulations in the United States (FAA, 2016), there is rapid growth in commercial UAS operations mapping existing infrastructure and construction activities. This study provides applicable results that operators can use with similar site characteristics.

Across the disciplines that have adopted UAS mapping technology, certain site characteristics are more prevalent than others within a given discipline. For resource extraction applications such as open pit mining where UAS are used to map removal of material from mine walls or volumetric computation of piles (Chen, Li, Chang, Sofia, & Tarolli, 2015; Tong et al., 2015), substantial topographic relief is common and expected. These areas with sharp changes in elevation and extreme topographic gradients may be more susceptible to errors in vertical accuracy when using digital elevation models generated from less rigorous processing parameters (e.g., 'low quality' dense clouds). In forestry applications, vegetated land cover and tree canopy density play significant roles in obscuring the ground surface for accurate elevation surface modeling during leaf on conditions (Dandois & Ellis, 2013). However, there is inherent variability in site characteristics within disciplines as well. For example, within the subdiscipline of coastal geomorphology, substantial topographic relief is common in cliff surveying (M. R. James & Robson, 2012; Westoby, Brasington, Glasser, Hambrey, & Reynolds, 2012) while low and moderate topographic relief is prevalent in beach monitoring (Casella et al., 2016; Gonçalves & Henriques, 2015). Given this variability in site characteristics within and across disciplines, additional investigation into the tradeoffs between processing time, spatial accuracy, and geometric quality is advised across a variety of topographic gradients and land cover types to avoid misapplication of the results reported herein.

Appropriate data acquisition techniques are critical to achieving optimal spatial accuracies of resultant UAS-derived geospatial datasets. Data acquisition is broadly categorized as either control or image acquisition. In this study, ground control was collected by precise measurement using a robotic total station. While total station surveying is a more accurate technique than the establishment of either ground or airborne control by GNSS surveying alone (Ghilani & Wolf, 2014), total station surveying is a more time intensive process over large survey areas with airborne GNSS being the least time intensive surveying technique. When considering the tradeoffs between field time and desired spatial accuracy, the accuracy of the input control is critical to the reproducibility and subsequent accuracy of the derived SfM datasets (Clapuyt et al., 2016). With input vertical and horizontal accuracies of less than 1 cm for both the ground control and checkpoints, this study reinforces the concept that the resultant horizontal and vertical geospatial dataset spatial accuracy is limited by the accuracy of the control (Toby N. Tonkin & Midgley, 2016). As mentioned earlier, site characteristics (e.g., closed canopies in forestry applications) can limit both the methods of control establishment as well as the upper threshold of expected spatial accuracy.

Both hardware (i.e., cameras) and flight planning operations can affect image acquisition and the subsequent spatial accuracy and geometric quality of UAS-derived geospatial datasets. In this study, the UAS platform flew at a consistent 55m AGL capturing near-nadir perspective imagery with a Sony A6000 non-metric camera. For non-metric cameras where self-calibration is needed, James et al. (2014) found that collecting convergent imagery could reduce doming error effects. Carbonneau et al. (2016) completed additional research with multiple non-metric cameras showing the cost effectiveness of collecting both nadir and oblique imagery at multiple altitudes in improving camera self-calibration parameters. The authors did not collect convergent imagery as part of this data acquisition but do consider this flight acquisition method (Carbonneau & Dietrich, 2016; Mike R. James & Robson, 2014) to be a worthy endeavor especially at the entry level end of the UAS market where camera self-calibration is required. Investigation into the impact that convergent imagery has on processing time and alignment processing time in particular is recommended in subsequent study. Further, considerable work related to camera self-calibration and UAS flight planning parameters has been completed within the geomorphology community thus far (Carbonneau & Dietrich, 2016; M. R. James et al., 2017; Mike R. James & Robson, 2014). Additional research into the impact flight planning characteristics have on the spatial accuracy and geometric quality of UAS-derived geospatial datasets in non-geomorphological applications (e.g., agriculture, forestry) is encouraged as well.

4.2. Data Processing

The computer hardware configuration described in Section 2.4 is representative of a typical desktop workstation that exceeds the minimum specifications set out in the Agisoft Photoscan manual (Agisoft, 2016). For each activated GPU, one CPU was subsequently deactivated per the manual. The GPUs are critical to processing time improvement due to Agisoft support of OpenCL acceleration during the depth maps reconstruction phase of building dense point clouds. The building dense clouds step is the most time intensive step as shown in Table 2. To estimate the impact that GPUs have on processing time during dense cloud generation, the authors conducted a small test using the parameters found in Table 9 with eight CPUs and zero GPUs activated (C8G0) versus seven CPUs and one GPU activated (C7G1). The total processing time and depth map generation processing time for C8G0 was 5:44:00 hrs and 5:00:00 hrs, respectively. Meanwhile, the total processing time and depth map generation processing time for C7G1 was 3:22:00 hrs and 2:35:00 hrs, respectively. On a per image basis (122 images total), the use of a CPU instead of a GPU resulted in an increase of 72 s/image in depth map generation processing time. This result highlights the importance of using at least one GPU to enhance processing time as supported by the literature (Agisoft, 2016; Verhoeven, 2011). Without access to more than one GPU, it is hypothesized that the depth map generation processing time as part of the dense point cloud generation step could be decreased with the substitution of additional GPUs for CPUs. Further investigation is needed to confirm the magnitude of the hypothesized decrease both within Photoscan and other SfM software packages that use GPUs (e.g., Pix4D (Pix4D, 2016), VisualSFM (Wu, 2016)).

Cloud and cluster computing continue to grow as options for processing large amounts of geospatial data (Li, Yang, Liu, Hu, & Jin, 2016; Sugumaran, Hegeman, Sardeshmukh, & Armstrong, 2015; Yang, Raskin, Goodchild, & Gahagan, 2010). However, internet accessibility, internet quality, and even finances can all hamper the availability of these robust computing resources for some operators and applications. For example, using UAS-derived orthophotos to delineate property boundaries in remote areas through participatory mapping requires a quick turnaround time from field collection to community-based exercises (Barnes & Volkmann, 2015). Data processing in remote areas is often without the benefit of high bandwidth internet for accessing cloud computing solutions (Turner et al., 2014). Thus, a mobile desktop or a laptop must be used to process the data. Ensuring that these mobile computer resources have at least one GPU is imperative for processing time efficiency.

For SfM software, this study exclusively examined Photoscan due to its wide adoption, extensive user community, affordable purchase price, and reporting features as outlined in Section 2.4. While further investigation of SfM processing time across multiple software packages is encouraged, literature (Turner et al., 2014) suggests that processing time using similar parameters is relatively the same between the two predominant SfM commercial software packages, Agisoft Photoscan (Agisoft, 2016) and Pix4D (Pix4D, 2016). The exact parameters recommended in Table 9 cannot be directly transferred to other software packages due to slightly different algorithms and implementations. The overarching results of this study are that image downscaling during alignment and dense cloud generation can yield significant time efficiency gains without sacrificing spatial accuracy in low to moderate topographic relief project sites. This broader result is reasonably transferrable based on the recent literature (Gross & Heumann, 2016) finding no statistically significant difference in spatial accuracy between the predominant SfM software packages.

As shown in Table 2, the overall processing time is primarily a result of two processing steps: the final alignment and the dense cloud generation parameters. While not nearly as time intensive as dense cloud generation, the final alignment step can substantially affect processing time depending upon the parameters selected. In this study, changing the alignment ‘accuracy’ of the default setting from ‘highest’ to ‘lowest’ resulted in a total time decrease from 0:50:20 hrs (‘highest accuracy’) to 0:02:39 hrs (‘lowest accuracy’) or a decrease in processing time of 23 s/image. With minimal variation in the horizontal and vertical spatial accuracy across all trials, the alignment parameters (e.g., ‘accuracy’, ‘keypoint limit’, ‘tiepoint limit’) had nominal impact on spatial accuracy for this study area.

The EXIF headers of the images used in this study lacked georeferencing information. Therefore, the ‘pair preselection’ parameter was disabled in Table 9. Consequently, the Photoscan software did not have any preconditions to assist with imagery alignment. This ‘disabled’ setting could be considered the worst case scenario for imagery alignment. Meanwhile, the best case scenario for imagery alignment with regards to ‘pair preselection’ is a ‘reference’ setting that uses precise camera exposure stations derived from phase-based differential GNSS processing. Using the settings found in Table 9 and an accurate post-processed kinematic (PPK) GNSS navigation trajectory of the camera exposure stations for this same study site, the authors found that changing to a ‘reference pair preselection’ alignment parameter yielded a decrease in processing time of 0.5 s/image. Likewise, changing the ‘accuracy’ parameter

in Table 9 from ‘low’ to ‘medium’ (i.e., less image downscaling) and using ‘reference pair preselection’ yielded a decrease in processing time of 1 s/image for the PPK GNSS camera exposure positions relative to a ‘disabled’ setting. For a dataset with a larger number of images, this time savings could prove beneficial; however, for this size project area, the time difference is small relative to other parameter settings. The real benefits of using precise airborne GNSS control are realized through time savings in the field (M. R. James et al., 2017) and for applications such as forestry where the placement of unobscured ground control is difficult (Dandois & Ellis, 2013). While differential GNSS positioning using carrier phase observations is gaining traction in the UAS community, most entry level UAS rely on code-based positioning (Carbonneau & Dietrich, 2016). The processing time benefits of using approximate non-differential, code-based GNSS camera positions fall between the precise PPK GNSS derived camera positions tested above and the lack of alignment preconditioning used in the overall study.

The most time intensive step in the SfM software processing is the dense point cloud generation as shown in Table 2. The authors varied the dense point cloud generation ‘quality’ parameter to test the effect image downscaling had on spatial accuracy, geometric quality, and processing time. Across all trials, the minimal variation in spatial accuracy suggests that image downscaling during dense point cloud construction had a marginal effect on the spatial accuracy of generated orthophotos and digital elevation models. Altering the ‘quality’ parameter yielded significant differences in processing time. The ‘ultra high quality’ setting was dismissed as an optimal setting since the dense cloud generation processing time was about 570 s/image for this study area. In comparison, the ‘high’, ‘medium’, and ‘low’ settings contributed an average dense cloud generation processing time across all trials of 86 s/image, 17 s/image, and 4 s/image, respectively. Therefore, it is clear that there are significant processing time gains that can be made from downscaling the input imagery at this step. Areas with sharp changes in elevation and extreme topographic gradients may require more stringent dense cloud generation parameters to maintain a level of spatial accuracy that is nearly equivalent to the accuracy of the input georeferencing control. Thus, agricultural applications with relatively flat topography (Caturegli et al., 2016) would be less likely to be impacted by the dense point clouds generated with ‘low quality’ settings than geomorphological applications in steeper terrain (M. R. James & Robson, 2012; Warrick, Ritchie, Adelman, Adelman, & Limber, 2016; Westoby et al., 2012) or with hummocky relief (Toby N. Tonkin & Midgley, 2016). Further investigation is needed with project sites in these steeper terrain areas to quantify the susceptibility of these areas to errors in vertical accuracy when using digital elevation models generated from lower density point clouds.

The results from the geometric quality assessment showed that there were significant reductions in image artifacts, image blur, and data voids when using ‘high quality’ dense cloud generation parameters instead of ‘medium quality’. Thus, the user needs to determine the tradeoff between enhanced qualitative fidelity of the derived geospatial datasets in terms of distinguishing and identifying features within the imagery versus the benefits of reduced processing time. For example, in disaster response applications (Pajares, 2015), faster processing times resulting in geospatial datasets with poorer spatial accuracies and less qualitative fidelity are more acceptable when the mapping products are used to quickly and effectively determine which houses are damaged and what areas might need immediate assistance. In forestry and ecological applications, the difference between classifying land cover by general classes versus specific species can lie in the qualitative fidelity of the resultant mapping products. For other applications such as infrastructure surveying (Colomina & Molina, 2014), higher accuracy mapping products with greater image fidelity may be needed for roadway design and construction. As with any UAS mapping project, client and end user needs dictate the benchmarks to set for spatial accuracy and geometric quality of the final geospatial datasets. The data acquisition techniques (i.e., control and image acquisition) and the rigorousness of the SfM processing parameters need to be tailored by the operator to meet these benchmarks.

5. Conclusions

This study sought a more time efficient Structure from Motion (SfM) processing approach for generating unmanned aerial system (UAS) derived geospatial datasets, specifically orthophoto mosaics and digital elevation models. To analyze the impact that SfM processing parameter selection had on spatial accuracy, geometric quality, and processing time, the representative SfM software package for image processing was Agisoft Photoscan v1.2.5. A MAP-M4 multirotor quadcopter with a 16mm Sony a6000 camera captured 122, ~1.25 cm/pixel ground resolution images of a study area in Alachua County, FL, USA. Spatial accuracy (i.e., horizontal and vertical difference between ground truth data and the final mapping products) and geometric quality (i.e., qualitative fidelity of the derived orthophoto mosaics in terms of distinguishing and identifying features within the imagery) were the primary characteristics evaluated in determining the tradeoff between processing time and the geospatial dataset accuracy and quality.

In low to moderate topographic relief locations, the results indicate that less rigorous Photoscan processing parameters, specifically alignment and dense cloud generation parameters, provide substantial time savings without sacrificing the spatial accuracy of UAS-derived geospatial datasets. Lower 'quality' parameters in the dense cloud building step of the UAS mapping workflow yield the greatest time savings. The 'high', 'medium', and 'low' 'quality' settings contributed an average dense cloud generation processing time across all trials of 86 s/image, 17 s/image, and 4 s/image, respectively. For projects with a large number of images, the impact of image downscaling at this step leads to significant processing time improvement. When considering geometric quality in addition to spatial accuracy, reductions in the alignment 'accuracy' and the 'key point limit' did not impact the spatial accuracy of the resultant geospatial datasets. To further enhance understanding of tradeoffs between processing time, spatial accuracy, and geometric quality of UAS derived geospatial datasets, recommendations for future work include applying the procedures and results found herein across a variety of both SfM software packages (e.g., Pix4D) and project sites (e.g., more extreme topographic gradients, differing land cover).

Acknowledgments

Acknowledgments: This is a collaborative study between the University of Florida (UF) Geomatics program and Micro Aerial Projects L.L.C. (<http://www.microaerialprojects.com/>). No external sources of funding were used to conduct this study. Thank you to Oliver Volkmann and Nicholas DiGruttolo for field data collection and UAS operations. Thank you to Levente Juhasz for assistance with automating data extraction.

REFERENCES

- Agisoft. (2016). Agisoft PhotoScan User Manual: Professional Edition, Version 1.2. Agisoft LLC. Retrieved from http://www.agisoft.com/pdf/photoscan-pro_1_2_en.pdf
- ASPRS. (1990, March). ASPRS Positional Accuracy Standards for Digital Geospatial Data. American Society for Photogrammetry and Remote Sensing. Retrieved from http://www.asprs.org/a/society/committees/standards/1990_jul_1068-1070.pdf
- ASPRS. (2015). ASPRS Positional Accuracy Standards for Digital Geospatial Data. *Photogrammetric Engineering & Remote Sensing*, 81(3), 53.
- Barnes, G., & Volkmann, W. (2015). High-Resolution Mapping with Unmanned Aerial Systems. *Surveying and Land Information Science*, 74(1), 5–13.
- CAA. (2016). The Air Navigation Order 2016 and Regulations (FAA News No. CAP 393) (p. 408). London, UK: Civil Aviation Authority. Retrieved from http://publicapps.caa.co.uk/docs/33/CAP393Ed5Am1_OCT2016_BM.pdf
- Carbonneau, P. E., & Dietrich, J. T. (2016). Cost-effective non-metric photogrammetry from consumer-grade sUAS: implications for direct georeferencing of structure from motion photogrammetry. *Earth Surface Processes and Landforms*, n/a-n/a. <https://doi.org/10.1002/esp.4012>
- Casella, E., Rovere, A., Pedroncini, A., Stark, C. P., Casella, M., Ferrari, M., & Firpo, M. (2016). Drones as tools for monitoring beach topography changes in the Ligurian Sea (NW Mediterranean). *Geo-Marine Letters*, 36(2), 151–163. <https://doi.org/10.1007/s00367-016-0435-9>
- Caturegli, L., Corniglia, M., Gaetani, M., Grossi, N., Magni, S., Migliazzi, M., ... Volterrani, M. (2016). Unmanned Aerial Vehicle to Estimate Nitrogen Status of Turfgrasses. *PLOS ONE*, 11(6), e0158268. <https://doi.org/10.1371/journal.pone.0158268>
- Chen, J., Li, K., Chang, K.-J., Sofia, G., & Tarolli, P. (2015). Open-pit mining geomorphic feature characterisation. *International Journal of Applied Earth Observation and Geoinformation*, 42, 76–86. <https://doi.org/10.1016/j.jag.2015.05.001>
- Clapuyt, F., Vanacker, V., & Van Oost, K. (2016). Reproducibility of UAV-based earth topography reconstructions based on Structure-from-Motion algorithms. *Geomorphology*, 260, 4–15. <https://doi.org/10.1016/j.geomorph.2015.05.011>
- Colomina, I., & Molina, P. (2014). Unmanned aerial systems for photogrammetry and remote sensing: A review. *ISPRS Journal of Photogrammetry and Remote Sensing*, 92, 79–97. <https://doi.org/10.1016/j.isprsjprs.2014.02.013>
- Dandois, J. P., & Ellis, E. C. (2013). High spatial resolution three-dimensional mapping of vegetation spectral dynamics using computer vision. *Remote Sensing of Environment*, 136, 259–276. <https://doi.org/10.1016/j.rse.2013.04.005>
- Dietrich, J. T. (2016). Riverscape mapping with helicopter-based Structure-from-Motion photogrammetry. *Geomorphology*, 252, 144–157. <https://doi.org/10.1016/j.geomorph.2015.05.008>
- ESRI. (2016). ArcGIS 10.4 for Desktop (ArcMap). Environmental Systems Research Institute, Inc. Retrieved from <https://desktop.arcgis.com/en/arcmap/10.4/>
- FAA. (2016). Summary of small unmanned aircraft rule (Part 107) (FAA News) (p. 3). Washington, DC: Federal Aviation Administration. Retrieved from https://www.faa.gov/uas/media/Part_107_Summary.pdf
- FGDC. (1998). Geospatial Positioning Accuracy Standards, Part 3: National Standard for Spatial Data Accuracy (NSSDA) (No. FGDC-STD-007.3-1998.) (p. 28). Reston, VA: Federal Geographic Data Committee. Retrieved from <https://www.fgdc.gov/standards/projects/accuracy/part3/chapter3>
- Flood, M. (2004). Vertical accuracy reporting for LiDAR data. American Society for Photogrammetry and Remote Sensing LiDAR Committee.
- Fonstad, M. A., Dietrich, J. T., Courville, B. C., Jensen, J. L., & Carbonneau, P. E. (2013). Topographic structure from motion: a new development in photogrammetric measurement. *Earth Surface Processes and Landforms*, 38(4), 421–430. <https://doi.org/10.1002/esp.3366>

- Gerke, M., & Przybilla, H.-J. (2016). Accuracy Analysis of Photogrammetric UAV Image Blocks: Influence of Onboard RTK-GNSS and Cross Flight Patterns. *Photogrammetrie - Fernerkundung - Geoinformation*, 2016(1), 17–30. <https://doi.org/10.1127/pfg/2016/0284>
- Ghilani, C. D., & Wolf, P. R. (2014). *Elementary Surveying: An Introduction to Geomatics* (14th ed.). Upper Saddle River, N.J: Pearson Education, Inc.
- Gonçalves, J. A., & Henriques, R. (2015). UAV photogrammetry for topographic monitoring of coastal areas. *ISPRS Journal of Photogrammetry and Remote Sensing*, 104, 101–111. <https://doi.org/10.1016/j.isprsjprs.2015.02.009>
- Gross, J. W., & Heumann, B. W. (2016). A Statistical Examination of Image Stitching Software Packages For Use With Unmanned Aerial Systems. *Photogrammetric Engineering & Remote Sensing*, 82(6), 419–425. <https://doi.org/10.14358/PERS.82.6.419>
- Harwin, S., & Lucieer, A. (2012). Assessing the Accuracy of Georeferenced Point Clouds Produced via Multi-View Stereopsis from Unmanned Aerial Vehicle (UAV) Imagery. *Remote Sensing*, 4(6), 1573–1599. <https://doi.org/10.3390/rs4061573>
- James, M. R., & Robson, S. (2012). Straightforward reconstruction of 3D surfaces and topography with a camera: Accuracy and geoscience application. *Journal of Geophysical Research: Earth Surface*, 117(F3), F03017. <https://doi.org/10.1029/2011JF002289>
- James, M. R., Robson, S., d'Oleire-Oltmanns, S., & Niethammer, U. (2017). Optimising UAV topographic surveys processed with structure-from-motion: Ground control quality, quantity and bundle adjustment. *Geomorphology*, 280, 51–66. <https://doi.org/10.1016/j.geomorph.2016.11.021>
- James, Mike R., & Robson, S. (2014). Mitigating systematic error in topographic models derived from UAV and ground-based image networks. *Earth Surface Processes and Landforms*, 39(10), 1413–1420. <https://doi.org/10.1002/esp.3609>
- Javernick, L., Brasington, J., & Caruso, B. (2014). Modeling the topography of shallow braided rivers using Structure-from-Motion photogrammetry. *Geomorphology*, 213, 166–182. <https://doi.org/10.1016/j.geomorph.2014.01.006>
- Li, Z., Yang, C., Liu, K., Hu, F., & Jin, B. (2016). Automatic Scaling Hadoop in the Cloud for Efficient Process of Big Geospatial Data. *ISPRS International Journal of Geo-Information*, 5(10), 173. <https://doi.org/10.3390/ijgi5100173>
- Messinger, M., Asner, G., & Silman, M. (2016). Rapid Assessments of Amazon Forest Structure and Biomass Using Small Unmanned Aerial Systems. *Remote Sensing*, 8(8), 615. <https://doi.org/10.3390/rs8080615>
- Pajares, G. (2015). Overview and Current Status of Remote Sensing Applications Based on Unmanned Aerial Vehicles (UAVs). *Photogrammetric Engineering & Remote Sensing*, 81(4), 281–330. <https://doi.org/10.14358/PERS.81.4.281>
- Paneque-Gálvez, J., McCall, M., Napoletano, B., Wich, S., & Koh, L. (2014). Small Drones for Community-Based Forest Monitoring: An Assessment of Their Feasibility and Potential in Tropical Areas. *Forests*, 5(6), 1481–1507. <https://doi.org/10.3390/f5061481>
- Pix4D. (2016). Pix4D mapper 2.2 Manual. Retrieved September 20, 2016, from <https://support.pix4d.com>
- Puliti, S., Olerka, H., Gobakken, T., & Næsset, E. (2015). Inventory of Small Forest Areas Using an Unmanned Aerial System. *Remote Sensing*, 7(8), 9632–9654. <https://doi.org/10.3390/rs70809632>
- RTKLIB. (2017). RTKLIB: An Open Source Program Package for GNSS Positioning. Retrieved March 27, 2017, from <http://www.rtklib.com/rtklib.htm>
- Sauerbier, M., Siegrist, E., Eisenbeiss, H., & Demir, N. (2011). The practical application of UAV-based photogrammetry under economic aspects. *International Archives of the Photogrammetry, Remote Sensing and Spatial Information Sciences*, 38(1). Retrieved from <http://www.int-arch-photogramm-remote-sens-spatial-inf-sci.net/XXX-VIII-1-C22/45/2011/isprsarchives-XXXVIII-1-C22-45-2011.pdf>
- Sugumaran, R., Hegeman, J. W., Sardeshmukh, V. B., & Armstrong, M. P. (2015). Processing remote-sensing data in cloud computing environments. In *Remotely Sensed Data Characterization, Classification, and Accuracies* (pp. 553–562). CRC Press. Retrieved from <http://www.crcnetbase.com/doi/pdf/10.1201/b19294-38>

- Tavani, S., Granado, P., Corradetti, A., Girundo, M., Iannace, A., Arbués, P., ... Mazzoli, S. (2014). Building a virtual outcrop, extracting geological information from it, and sharing the results in Google Earth via OpenPlot and Photoscan: An example from the Khaviz Anticline (Iran). *Computers & Geosciences*, 63, 44–53. <https://doi.org/10.1016/j.cageo.2013.10.013>
- Tong, X., Liu, X., Chen, P., Liu, S., Luan, K., Li, L., ... Hong, Z. (2015). Integration of UAV-Based Photogrammetry and Terrestrial Laser Scanning for the Three-Dimensional Mapping and Monitoring of Open-Pit Mine Areas. *Remote Sensing*, 7(6), 6635–6662. <https://doi.org/10.3390/rs70606635>
- Tonkin, T. N., Midgley, N. G., Graham, D. J., & Labadz, J. C. (2014). The potential of small unmanned aircraft systems and structure-from-motion for topographic surveys: A test of emerging integrated approaches at Cwm Idwal, North Wales. *Geomorphology*, 226, 35–43. <https://doi.org/10.1016/j.geomorph.2014.07.021>
- Tonkin, Toby N., & Midgley, N. G. (2016). Ground-Control Networks for Image Based Surface Reconstruction: An Investigation of Optimum Survey Designs Using UAV Derived Imagery and Structure-from-Motion Photogrammetry. *Remote Sensing*, 8(9), 786. <https://doi.org/10.3390/rs8090786>
- Turner, D., Lucieer, A., & Wallace, L. (2014). Direct Georeferencing of Ultrahigh-Resolution UAV Imagery. *IEEE Transactions on Geoscience and Remote Sensing*, 52(5), 2738–2745. <https://doi.org/10.1109/TGRS.2013.2265295>
- Verhoeven, G. (2011). Taking computer vision aloft – archaeological three-dimensional reconstructions from aerial photographs with photoscan. *Archaeological Prospection*, 18(1), 67–73. <https://doi.org/10.1002/arp.399>
- Wallace, L., Lucieer, A., Malenovský, Z., Turner, D., & Vopěnka, P. (2016). Assessment of Forest Structure Using Two UAV Techniques: A Comparison of Airborne Laser Scanning and Structure from Motion (SfM) Point Clouds. *Forests*, 7(3), 62. <https://doi.org/10.3390/f7030062>
- Warrick, J. A., Ritchie, A. C., Adelman, G., Adelman, K., & Limber, P. W. (2016). New Techniques to Measure Cliff Change from Historical Oblique Aerial Photographs and Structure-from-Motion Photogrammetry. *Journal of Coastal Research*. Retrieved from <http://www.jcronline.org/doi/abs/10.2112/JCOASTRES-D-16-00095.1>
- Westoby, M. J., Brasington, J., Glasser, N. F., Hambrey, M. J., & Reynolds, J. M. (2012). “Structure-from-Motion” photogrammetry: A low-cost, effective tool for geoscience applications. *Geomorphology*, 179, 300–314. <https://doi.org/10.1016/j.geomorph.2012.08.021>
- Wolf, P. R., & Dewitt, B. A. (2000). *Elements of Photogrammetry : with Applications in GIS*. Boston: McGraw-Hill.
- Wu, C. (2016, September 20). VisualSfM : A Visual Structure from Motion System. Retrieved from <http://ccwu.me/vsfm/>
- Yang, C., Raskin, R., Goodchild, M., & Gahegan, M. (2010). Geospatial Cyberinfrastructure: Past, present and future. *Computers, Environment and Urban Systems*, 34(4), 264–277. <https://doi.org/10.1016/j.compenurbsys.2010.04.001>